PCCP

Accepted Manuscript

ROYAL SOCIETY OF CHEMISTRY

www.rsc.org/pccp

ARTICLE TYPE

Effect of TiO_2 particles on normal and resonance Raman spectra of Coumarin 343: A theoretical investigation†

Linzhi Yang,[a] Wenpeng Wu,[b] and Yi Zhao*[a]

It is well known that interfacial structures and charge transfer in dye-sensitized solar cells are extremely important for the enhancement of cell efficiency. Here, the normal Raman spectra (NRS) and resonance Raman spectra (RRS) of a C343-sensitized TiO_2 cluster (Ti_9O_{18}) are theoretically predicted from combined electronic structure calculations and vibrationally-resolved spectral method to reveal the relationship between interfacial geometries and excited-state dynamics. The results show that although the NRS of both the free C343 and C343-TiO_2 cluster correspond to the vibrational motions of C343 in a high frequency domain, their mode frequencies show obvious differences due to the interaction of TiO_2 cluster on C343, and several new Raman active fingerprint modes, such as bidentate chelating bonding modes, can be used to determine interfacial geometries. However, the resonance Raman activities of low-frequency modes are significantly enhanced and several modes from the TiO_2 cluster can be observed, consistent with experimental measurement. Furthermore, the RRS from a local excited state and a charge transfer state of C343-TiO_2 are dramatically different, for instance, new Raman active modes with 1212 cm^{-1}, 1560 cm^{-1} and 1602 cm^{-1}, corresponding to the motions of CH_2 rocking, C=C/C-N/C=O stretching and C=O/C=C stretching, appear from the charge transfer state. The obtained information of mode-specific reorganization energies from these excited states are greatly helpful to understand and control interfacial electron transfer.

1 Introduction

Dye-sensitized solar cells (DSSCs) have attracted a great attention over the past decades due to their low cost and relatively high light-to-electricity conversion efficiency [1–5]. DSSCs are based on transition metal complexes or organic dye molecules that adsorbed on a semiconductor, such as titanium dioxide (TiO_2). Commonly, the ground states of chromophores are located within the band gap of TiO_2, and the photo-induced excited states are in resonance with the conduction band of semiconductor. It is now known that photo-induced ultrafast charge transfer (CT) at the interface of chromophore and semiconductor is an important process for the enhancement of solar energy conversion efficiency. Accordingly, this CT process has been extensively investigated, and two possible CT ways are suggested. The first one is that a photo absorption creates the excited state of adsorbed molecule and sequentially the excited-state electron injects into the conduction band [6–10]. The second one is that a photo excitation directly generates a CT state in which the electron and hole are distributed on the TiO_2 and chromophore, respectively [11–14]. Theoretically, either the full quantum mechanism based on modeling Hamiltonians [15–19] or mixed quantum-semiclassical (classical) methods on explicit atomistic simulations [10,20–23] has been proposed to investigate real time charge transfer dynamics, and most results point to the first mechanism of charge transfer.

On the other hand, resonance Raman spectra (RRS) have also been proposed to investigate the electron injection process. RRS essentially provide a good estimate of vibrational frequencies and reorganization energies (see, for instance, references [24–27]). The analysis of RRS intensities can obtain excited state dynamics in a subpicosecond time scale and describe photo-induced ultrafast mode-specific CT processes. Indeed, several experiments [28–30] have measured the RRS from the CT state, which has been modeled from the time-dependent wave packet propagation formulism [25,31]. However, it has been demonstrated that the first CT mechanism at the interface mentioned above is a favorable way for most dye sensitized TiO_2 nanoparticles [8,10,23,32–36], and the RRS from a local excited state of dye-sensitized systems should have a different property from a CT state. In this paper, we therefore investigate RRS from both the local excited state and CT state to reveal detailed information to understand CT dynamics.

In our previous work [37], we have calculated the normal Raman spectra (NRS) and RRS of Coumarin 343 (C343) molecule and found that both the NRS and RRS are suitable tools to identify the different isomer structures of C343 because the spectral intensity is very sensitive to C343 geometries. Here, we take C343-TiO_2 as an example for the present purpose due to our knowledge for the RRS of C343, and available experimental RRS [38] for comparison. Unlike a single C343 molecule, the density of C343-TiO_2 excited states is commonly very high, leading to a difficulty to opti-

[a] *State Key Laboratory of Physical Chemistry of Solid Surfaces, Collaborative Innovation Center of Chemistry for Energy Materials, Fujian Provincial Key Lab of Theoretical and Computational Chemistry, and College of Chemistry and Chemical Engineering, Xiamen University, Xiamen, 361005, P. R. China. E-mail: yizhao@xmu.edu.cn*
[b] *Institute of Environmental and Analytical Sciences, College of Chemistry and Chemical Engineering, Henan University, Kaifeng, 475001, P. R. China*

mize the geometries of different excited states. Furthermore, it is still a challenge in present electronic structure methods to calculate the mode-specific reorganization of TiO_2 semiconductor required in RRS, because of too many atoms involved. Fortunately, several investigations[39,40] have shown that a small cluster TiO_2 (Ti_9O_{18}) can essentially catch the dominant energy-level property of C343-TiO_2 system. We thus use the similar TiO_2 cluster model to mimic the behaviors of TiO_2 semiconductor, and the vertical gradient method is adopted to estimate the mode-specific reorganizations to avoid the difficulty for the optimization of excited-state geometries. In spite of these simplified calculations, it is expected that RRS should reveal the key interfacial structures between C343 and TiO_2 particle and detailed information for understanding CT processes.

In the concrete implementations, we first construct several interfacial structures between C343 and TiO_2 cluster, and then use the NRS to reveal interfacial geometric information. In the electronic structure calculations for excited states, suitable quantum chemistry methods have to be carefully chosen to correctly obtain the structure parameters because the CT states are commonly involved in the C343-TiO_2 system. Although wavefunction-based approaches have a high-level accuracy, they are still meeting a numerical challenge in the present application. We thus adopt density functional theory (DFT) and time-dependent DFT (TDDFT) with suitable functionals to calculate electronic structure information to incorporate the long-range CT interaction. With the obtained structure parameters, the NRS can be easily obtained from Guassian software. In the calculation of RRS, the excited-state dynamics is required. Here, we will use the quantum correlation function method which has an analytical expression under a harmonic oscillator model[41].

The paper is organized as follows. Section 2 outlines the expression for the calculation of RRS and electronic structure methods for the calculations of geometric parameters. Section 3 illustrates results including the geometries, NRS and RRS. Concluding remarks are given in Section 4.

2 Computational methods

2.1 Resonance Raman spectra

In order to calculate RRS, one needs to know the Hamiltonian of two electronic states

$$H = |g\rangle H_g \langle g| + |e\rangle (H_e + \omega_{eg} - i\gamma)\langle e|. \quad (1)$$

Here, $|g\rangle$ and $|e\rangle$ represent the electronic ground and excited states, respectively. ω_{eg} is the difference between the potential energy minima of the two electronic states. γ is the factor related to the $|e\rangle$-state lifetime. Under the harmonic oscillator approximation, the nuclear Hamiltonians of electronic ground and excited states can be written as

$$H_g = \frac{1}{2}\sum_j^N (P_{g_j}^2 + \omega_{g_j}^2 Q_{g_j}^2), \quad (2)$$

$$H_e = \frac{1}{2}\sum_j^N (P_{e_j}^2 + \omega_{e_j}^2 Q_{e_j}^2), \quad (3)$$

where Q are the mass-induced nuclear coordinates and P are the corresponding momentum, ω_j is the vibrational frequency of the j-th mode. The normal-mode coordinates of ground and excited states are correlated by Duschinsky rotation matrix S by $Q_e = SQ_g + D$. D is the displacement between the equilibrium configurations of two electronic states. The eigenvalue and eigenwavefunction of vibrational Hamiltonian are labeled by $(n_{g,e} + 1/2)\hbar\omega_{g,e}$ and $|n_{g,e}\rangle$, respectively.

The differential photon scattering cross section of RRS is given by[42]

$$\sigma(\omega_L, \omega_S) = \frac{4\omega_L \omega_S^3}{9c^4} S(\omega_L, \omega_S). \quad (4)$$

Here, ω_L and ω_S denote the frequencies of incident and scattering photons. c is the speed of the light, and the resonance Raman line shape $S(\omega_L, \omega_S)$ is given by the Kramers-Heisenberg-Dirac expression[43]

$$S(\omega_L, \omega_S) = \sum_{n_g, m_g} P_{n_g} I_{n_g, m_g}(\omega_L)\delta(\omega_S - \omega_L - \varepsilon_{n_g} + \varepsilon_{m_g}), \quad (5)$$

where P_{n_g} is the thermal population distribution on the ground state, and I_{n_g,m_g} is the Raman excitation profile from the vibrational state $|n_g\rangle$ to $|m_g\rangle$, and it has the following expression in a time domain

$$I_{n_g,m_g} = 2\pi \left| \int_0^\infty dt e^{i(\omega_L - \omega_{eg} + \varepsilon_{n_g})t - \gamma t} \times C_{mn}(t) \right|^2 \quad (6)$$

with the correlation function

$$C_{mn}(t) = \langle g, m_g | \mu e^{-iH_e t} \mu | g, n_g \rangle, \quad (7)$$

where μ is the transition dipole moment. The key step for RRS calculations, therefore, is to propagate the excited-state wavefunction $\mu|g, n_g\rangle$ generated by laser excitation. There are considerable approaches to do it[24–26,44]. Under the Condon approximation, these correlation functions have analytical solutions[41]. Thus, once the correlation functions are known, RRS can be easily obtained by Fourier transforms. In the present system, the vertical gradient approximation is adopted to get the coordinate shift D, which hints that the Duschinsky rotation matrix S is unit and the mode frequencies in ground and excited states are the same. By introducing a coordinate transform $\bar{Q} = Q/\sqrt{\omega}$, one can express $C_{mn}(t)$ by

$$C_{mn}(t) = \exp[f(t)\bar{D}^2](m!n!2^{m+n})^{-1/2}[\beta(t)]^{m+n} \sum_{k=0}^{k^*} \frac{(2k)!}{k!}\eta_{mnk} \times H_{m+n-2k}[f(t)\bar{D}/\beta(t)], \quad (8)$$

where

$$f(t) = -\frac{1}{2}[1-\exp(-i\omega_g t)], \quad (9)$$

$$\beta(t) = [-\frac{1}{2}\exp(-i\omega_g t)]^{1/2}, \quad (10)$$

$$\eta_{mnk} = \sum_{q=0}^{2k}(-1)^q C_m^{2k-q} C_n^q, \quad (11)$$

with

$$C_m^l = \frac{m!}{l!(m-l)!}. \quad (12)$$

2.2 Electronic structure methods

It is known that long-range corrected hybrid density functionals in (TD)DFT can reasonably describe the electronic structure and excited states with delocalized charge distributions. For the present systems, we find that the CAM-B3LYP functional[45–49] are suitable to describe the CT states of C343-TiO_2. In the geometric optimizations, frequency and vertical excitation energy calculations, we thus use the (TD)DFT/CAM-B3LYP/6-31+G** except that the efficient core potential LanL2DZ basis set is adopted for Ti atoms. The obtained frequencies are scaled by a factor of 0.964. Meanwhile, we also use conductor-like polarizable continuum model (CPCM)[50,51] to consider the solvent effect on geometries and excitation energies. All the quantum chemical calculations are performed with a Gaussian09 programme package[52].

The displacement D and Duschinsky rotation matrix S can be calculated from a project technique[53–55] by $D = L_e^T d$ and $S = L_e^T L_g$, where L_g and L_e correspond to the transform matrix for ground and excited states, respectively, which are obtained by the diagonalization of mass-weighted Hessian matrix H as $L^T H L = \omega^2$. $d(= x_g - x_e)$ is the corresponding shift, where x_g and x_e represent the mass-weighted coordinates of optimal ground and excited electronic states. As mentioned above, it is not easy to optimize the excited states of C343-TiO_2 because the most excited states are nearly degenerate. Here, we use a vertical gradient approximation[56,57] where it is assumed $\omega_e^j = \omega_g^j$, and $L_e = L_g$. This approximation has been demonstrated to be reasonable for absorption, antiresonance and RRS[58]. In this case, we easily find from Eq. (3) that $D_j = \omega_j^{-2}\frac{\partial V_e}{\partial Q_j}$, where V_e is the excited-state energy at the optimized ground-state geometry. By using the transform matrix L_g, we get

$$D_j = \sum_i (\omega_j)^{-2}(\frac{\partial V_e}{\partial x_i})L_g^{ij}. \quad (13)$$

3 Results and discussion

3.1 Geometries and electronic structures of C343-TiO_2

In C343-TiO_2, the interface geometry is extremely important for charge separation in solar cells. However, it is a challenge to theoretically construct the suitable interface arrangement because of too many possibilities. Fortunately, several available geometries of C343 and TiO_2 are helpful for us to build the favorable interface structures. We have investigated several C343 isomers[37], some of which are denoted as Ca, Cb and Cc as shown in Fig. 1. It displays that the relative ground-state energies of different isomers are nearly independent of the N-ring conformers (*anti*- and *syn*-), and they are basically determined by the -COOH conformers[37]. For instance, the isomer Ca with an intramolecular H-bond have a lower energy than Cb and Cc. We also find that *anti*-C343 isomers have lower ionization energies than *syn*-isomers. Here, we thus choose the C343 isomers with low ionization energies because the electron can transfer from them to TiO_2 easily. For TiO_2, a cluster model[59–63] has also been proposed to mimic its electronic and optical properties, and this model should be very suitable for the present purpose, because it allows us to detailed investigate the effect of possible interface bond structures with C343 on vibrationally-resolved spectra. Here, we use the Ti_9O_{18} cluster and its geometry and property of electronic structure are available[40,64–67].

Based on previous studies[4,10,68–75], six possible interfacial structures are constructed via the C=O and C-O bonds in C343 connected to the TiO_2 cluster, and the optimized geometries are shown in Fig. 1 as 1a, 1b, 1c, 2a, 2b and 2c, respectively. It is noted that the dissociated proton is attached to the oxygen of cluster terminal Ti-O bond to keep the system electro-neutral, and their positions are labeled in Fig. 1 by blue. Therein, 1a, 1b and 1c represent the monodentate interfaces, whereas 2a, 2b and 2c have bidentate structures, in which 2a and 2b are bidentate chelating to a single metal atom of TiO_2 cluster and 2c is bidentate bridging to two titanium atoms. In all six geometries, the Ti-O bond lengths between C343 and Ti_9O_{18} cluster change in the range of 1.8-2.3 Å, but the C-N bond lengths are very close to those of C343 itself. Those different conformers may result in different thermodynamical stability. From the energies of optimized ground states shown in Table 1, we indeed find that 1a, 2a and 2b are more stable than other conformers. The stability is closely related to the different adsorbtion among monodentate, bidentate chelating and bidentate bridging, also the different ring tensions between six-membered ring and four-membered ring. For instance, the bidentate chelating 2a and 2b are more stable than monodentate 1a, 1b and 1c. 2c is bidentate bridging to two titanium atoms in the six-membered ring, and the atom Ti with a large radium enhances the ring tension of six-membered ring, lead-

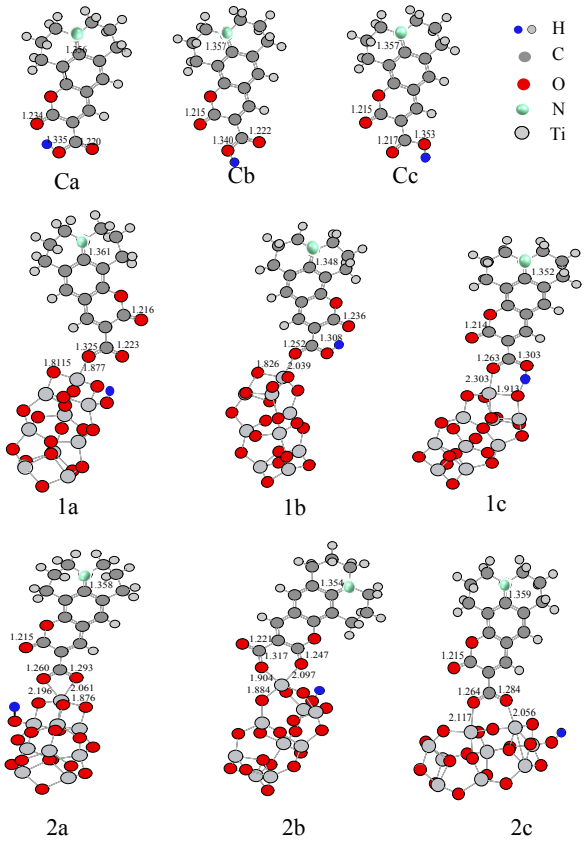

Fig. 1 The optimized structures of C343 attached to TiO_2

Table 1 Relative energies of different conformers of C343-Ti_9O_{18} (in eV)

Conformer	1a	1b	1c	2a	2b	2c
Relative energies	0.08	0.26	0.25	0.06	0	0.52

ing to the highest ground-state energy.

In DSSCs, the energy levels of the highest occupied molecular orbital (HOMO) and the lowest unoccupied molecular orbital (LUMO) of dye molecules and semiconductors are commonly used to judge whether photo-generated excitons dissociate or not at the interface. We thus calculate the HOMO and LUMO energies of C343, Ti_9O_{18} and their complex C343-Ti_9O_{18} in different conformers and the corresponding schematic picture is shown in Fig. 2. Obviously, both the LUMO and HOMO energies of C343 are higher than those of Ti_9O_{18} cluster, manifesting that small cluster model of Ti_9O_{18} can essentially catch the dominant energy scheme in DSSCs. It is noted that the calculated LUMO-HOMO energy gap of Ti_9O_{18} cluster is larger than that of TiO_2 semiconductor. This large energy gap may come from both the small cluster model and the functional in DFT calculation. It is well known that CAM-B3LYP functional overestimates the LUMO-HOMO energy gap. Indeed, the B3LYP functional predicts the band gap of 4.6 eV, closer to the experimental value. However, we find that B3LYP functional gives out an incorrect photo absorption property in the C343-TiO_2. We thus still use CAM-B3LYP to calculate the electronic structures of excited states because it is suitable to describe charge transfer states.

For six C343-TiO_2 complexes, although the HOMOs essentially come from C343 and the LUMOs are dominantly from TiO_2, their orbital energies are different. After careful comparison, we find that these complexes can be classified into two types, type one includes 1b, 1c and 2b, and type two are 1a, 2a and 2c. Obviously, type one has lower HOMO energies than type two, resulting in the larger LUMO-HOMO energy gaps. Further analysis reveals that the HOMO energy levels heavily depend on the charge distributions in C343 and TiO_2 fragments. Typically, the positive charge in TiO_2 leads to a higher HOMO energy level than the negative charge. Whether the charge is positive or negative in TiO_2 is closely related to the proton position. For instance, in the 1a conformer with the highest HOMO energy, the proton is bonded on the TiO_2 fraction and resulting charge is +0.59 *e* whereas the proton in 1b conformer is remained in C343 and the charge in TiO_2 becomes -0.20 *e*. We thus expect that the proton position can be used to control the HOMO energy levels.

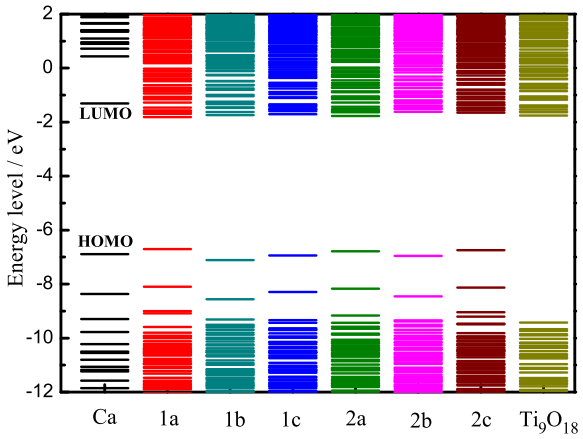

Fig. 2 Energy levels of C343, Ti_9O_{18} and different conformers of C343-Ti_9O_{18}

Although the HOMO and LUMO energy levels are useful to understand CT processes, the charge transfer rate is essentially determined by electronic states, and electronic absorption spectra are important to reveal excited-state properties and interfacial interactions. Fig. 3(a) displays the calculated absorp-

tion spectra of C343 (Ca geometry) and its six conformers with TiO_2. The first vertical excitation energies and corresponding oscillator strengths of these geometries are listed in Table 2. For the C343 molecule, the first peak of absorption corresponds to the excitation from the ground state to the first excited state, and the second excited state well separates from the first exited state. As the C343 is adsorbed on TiO_2, the spectral shapes do not have obvious changes and the first peak mainly corresponds to the local excitation of C343. However, the peak positions are obviously different from that of C343, and most peaks are red-shift with slightly higher intensities. The property has been confirmed by the experimental measurement[36,38,76]. Fig. 3(b) displays the comparisons of calculated spectra of C343 (Ca) and C343-TiO_2 (2b) with experimental spectra[38]. The calculated spectra with 50 nm red-shift, due to CAM-B3LYP's behavior of overestimating vertical excitation energy, are consistent with an experimental measurement, manifesting that the properties of excited states are correctly described by the present calculations. It is noted that the calculated absorption intensities in a high energy regime are lower than those from the experiments. This difference may be from the approximation that the vibrational effect is not incorporated. Our previous investigation[37] indeed indicates that the vibrational contribution can enhance the absorption intensity in that energy regime.

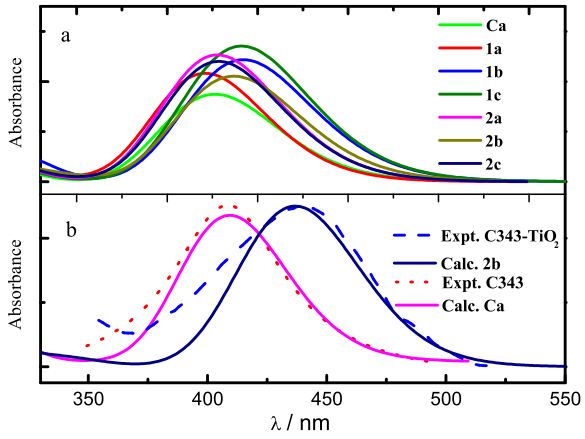

Fig. 3 (a) Absorption spectra of C343 and C343-Ti_9O_{18} and (b) comparison with experimental values

Based on the above interface geometries and electronic structure properties, Raman spectra can be further calculated to build the relationship between vibrational motions and spectra as well as to investigate excited-state dynamics. All the Raman spectra are calculated in a methanol solution for the purpose of comparison with experimental measurments[38].

Table 2 The first vertical excitation energies (E, in eV) and corresponding oscillator strengths (f) of different conformers.

Conformer	Ca	1a	1b	1c	2a	2b	2c
E	3.29	3.34	3.16	3.17	3.27	3.21	3.28
f	0.86	1.07	1.20	1.34	1.27	1.04	1.19

3.2 Normal Raman spectra (NRS)

The NRS essentially represent the vibrational information in the electronic ground state specific to the chemical bonds and symmetry of molecules. Fig. 4 displays the NRS for both the C343 isomers and the TiO_2 cluster. For C343 isomers, their Raman spectra are very similar. The modes with low frequencies (< 1000 cm^{-1}) are weak Raman-active, which dominantly correspond to ring breathing vibrations. The high-frequency modes have strong Raman activity. Within 1000-1600 cm^{-1}, the modes come from the vibrations of the parent ring of coumarin and N-ring, C-C and C-O stretching bonds, and CH_2 deformative motion, the coupled vibrations of C-C, C=C, C-N stretching motions and the scissoring vibrations of H atoms in plane are in 1500-1600 cm^{-1}, and the vibrations of -COOH group and carbonyl group in 1600-1800 cm^{-1}.

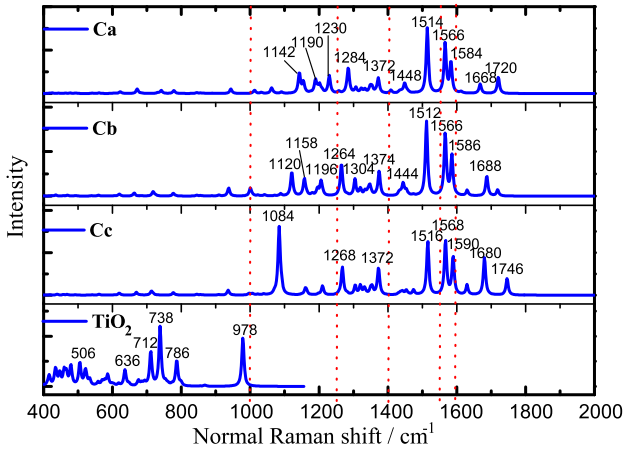

Fig. 4 The normal Raman spectra of several C343 isomers and TiO_2 cluster

Although the NRS for three isomers are similar, we can still find the feature modes to distinguish the isomer structures. For instance, the mode with 1084 cm^{-1} in the Cc isomer has a strong Raman activity, which represents the bond vibration of C-O in -COOH group of Cc isomer, whereas the Raman-active mode with 1720 cm^{-1} corresponds to the motion of C=O in -COOH group of Ca isomer.

For the Ti_9O_{18} cluster, however, the dominant Raman-

active modes are in the low frequency regime, and most of them represent the ring-deformed vibrational motions. The mode with high frequency of 978 cm^{-1} is ascribed as terminal Ti-O bond stretching vibration. It is noted that the NRS of this cluster is very different from that of anatase or rutile crystal[68,77–80], manifesting the importance of size effect of TiO_2.

After C343 is adsorbed on TiO_2, the NRS of the six complexes, shown in Fig. 5, are different due to their specific interface structures. The Raman-active modes are still in the high frequency regime, and they mainly correspond to the vibrational motions of C343 fragment and interface. However, these NRS are very different from those of C343 isomers. From the above analysis of charge distributions on C343 and TiO_2 fragments, it is known that C343 fragments in 1b ad 1c conformers have positive charges whereas others have negative charges. We thus expect that the NRS in C343 fragments correspond to those of C343 ions. Indeed, the NRS of the modes with the frequencies between 1400 to 1600 cm^{-1} in 1b and 1c, corresponding to the bond vibrations in the ring of C343, are similar to each other and different from others.

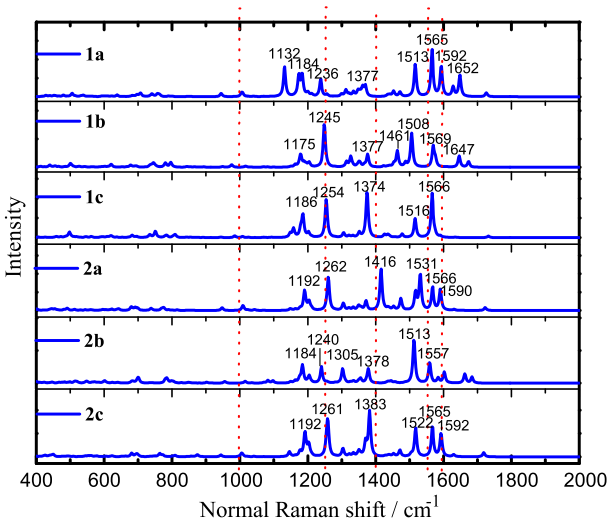

Fig. 5 The normal Raman spectra of C343-TiO_2 conformers

The Raman activity especially corresponding to C=O in -COOH group connecting to TiO_2 fragment becomes weak comparing with those in C343 itself. However, several fingerprint modes for the determination of interface structures appear. For instance, the C-O vibrational mode in the interface with 1132 cm^{-1}, corresponding to the mode with 1084 cm^{-1} of C343, has a strong Raman activity in the 1a conformer. The C-C vibrational modes, which only show in the interface with 1374 cm^{-1}, 1383 cm^{-1} and 1416 cm^{-1} for 1c, 2c, and 2a, respectively, have strong Raman activity. The mode with 1647 cm^{-1}, originally corresponding the C=O bond of -COOH group in C343, can be used to denote 1b isomer because it represents the C-O bond in the interface.

3.3 Resonance Raman spectra (RRS)

Compared to the NRS, the RRS are closely related to electronic excited-state dynamics. The mode-specific RRS intensities from different excited states are useful to determine the different properties of excited states. From the absorption spectra investigated above, we know that the first excited states (S_1) of C343-Ti_9O_{18} have similar properties to those of C343 isomers. We thus calculate the RRS for both C343 and C343-Ti_9O_{18} systems by using the incident laser frequency equaling to the vertical excitation energy of those states. The results are shown in Fig. 6 and Fig. 7, respectively.

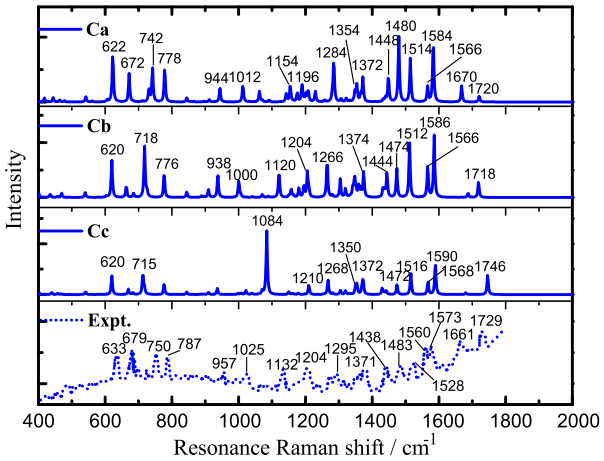

Fig. 6 The resonance Raman spectra of C343 isomers as well as the experimental values

It is seen that the RRS of C343 isomers display obvious differences from the NRS. Although the high-frequency modes still have Raman activities, similar to the NRS, but with different strengths, the RRS intensities in the low frequencies (400-1000 cm^{-1}) are significantly enhanced. These low-frequency modes mostly correspond to ring breathing, deformation and CH_2 deformation vibrations, manifesting that the rings have the obvious contribution to the excitation, which is confirmed by the π-π transition of the first excited state. Interestingly, the C-O vibrational mode in -COOH group of Cc isomer with 1084 cm^{-1} has a large Raman activity in both the RRS and NRS, and this mode can be used to identity the Cc isomer. In Fig. 6, we also display the experimental RRS[38]. It is found the RRS from the Ca isomer are the most close to the experimen-

tal measurement, for instance, the calculated low-frequency modes 622 cm^{-1},672 cm^{-1},742 cm^{-1} and 778 cm^{-1} correspond to 633 cm^{-1}, 679 cm^{-1}, 750 cm^{-1} and 787 cm^{-1} in the experiment[38], respectively; the calculated high-frequency mode 1584 cm^{-1} corresponds to 1573 cm^{-1} in the experiment[38]. This conclusion is also consistent with the stability analysis that the Ca isomer has the lowest ground-state energy.

After C343 is adsorbed on TiO_2, although the RRS of low-frequency modes are observable, they are suppressed comparing with those of C343 isomers. A possible reason can be explained by the different charge distributions on C343. It is known that the C343 isomers are neutral, however, the charges on C343 fragment in the C343-TiO_2 ground state are about 0.2-0.7 *e*, and these charges do not change too much in their excited states. Interestingly, the low-frequency modes with strong Raman activity still dominantly correspond to the coupled vibrational motions of ring deformations in C343 fragment, and only few modes of TiO_2 fragment are Raman activity, for instance, the only Ti-O stretching motion is observed at about 620 cm^{-1}. In the high-frequency domain, a slightly more modes become Raman active in RRS than those in NRS, and there are additional modes appearing at 1488 cm^{-1} (mainly C=C stretching coupling with CH_2 scissoring), 1584 cm^{-1} (coupling of C=C, C-C stretching and H in plane wagging), 1684 cm^{-1} (C=O stretching vibration in -COOH group). However, the modes with 1240 cm^{-1} and 1557 cm^{-1} of NRS disappear in RRS.

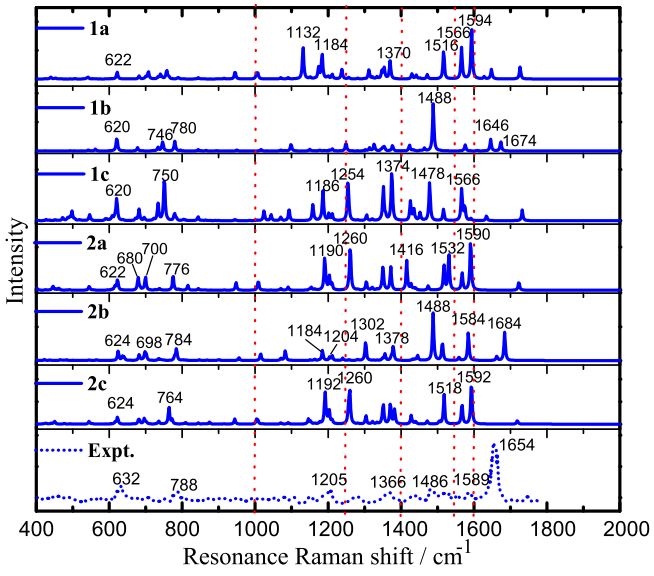

Fig. 7 The resonance Raman spectra of C343-TiO_2 conformers

Compared with the experiment[38], the RRS from 2b conformer basically match the experiment values. For example, 784 cm^{-1} and 1378 cm^{-1} correspond to 788 cm^{-1} and 1366 cm^{-1} in the experiment[38], respectively. Although the calculated RRS intensity for the modes with 1488 cm^{-1} and 1584 cm^{-1} are obviously stronger than the experimental measurement, and the intensities of other modes, such as low-frequency Ti-O mode and high-frequency C=O mode, are correctly predicted in the calculations. The rigorous prediction of RRS intensities requires to consider the charge transfer dynamics from C343 to TiO_2 fragment[81]. However, the present cluster model essentially catches the dominant property of the C343-TiO_2 exited state.

Now, we focus on the RRS of C343-TiO_2 from a charge transfer state. Here, the 2b conformer is taken as an example because its RRS is similar to the experimental one. As discussed above, the first excited state of C343-TiO_2 dominantly corresponds to the excitation of C343 fragment. The detailed analysis reveals that the transition of the first excited state comes from HOMO to LUMO+1 and LUMO+3, and these orbitals are displayed in Fig. 8. We further calculate several higher excited states and find out the S_2 state having charge transfer property with 0.5 *e* on C343 fragment transferred to TiO_2 fragment. The transition is mainly from HOMO to LUMO+2, LUMO+7 and LUMO+11, and such orbitals are also shown in Fig. 8. Obviously, the S_1 and S_2 states represent the local excited-state and charge transfer state, respectively.

We then calculate the RRS from the S_2 state, and the results are displayed in Fig. 9 together with the RRS from the S_1 state. It is found that there are only a few modes such as 1184 cm^{-1}, 1302 cm^{-1} and 1684 cm^{-1} appearing in the RRS from both the states, and the others from S_2 state are obviously different. Several low-frequency modes from the TiO_2 fragment become observable. For instance, the modes with 702 cm^{-1} and 742 cm^{-1} come from the vibrational motions of Ti-O bonds. In the high frequency, the new peaks with 1212 cm^{-1}, 1560 cm^{-1} and 1602 cm^{-1} correspond to the visional motions of CH_2 rocking, C=C/C-N/C=O stretching and C=O/C=C stretching, respectively, and the peak with 1488 cm^{-1} disappears although its intensity from the S_1 state is very strong. These differences of RRS may be applied to understand the charge transfer process from the local excited state to charge transfer state. It is known that the intensities of mode-specific RRS are proportional to the square of shifts *D*. The different intensities of RRS from two excited states manifest that the equilibrium positions of modes on these states are different from each other. Thus the behaviors of these modes are greatly helpful for us to understand and control the electron injection from C343 into conduction band of TiO_2 because the shifts of these modes on two excited states have obvious contribution to the reorganization energy for charge transfer. It should be noted that the calculated RRS from the

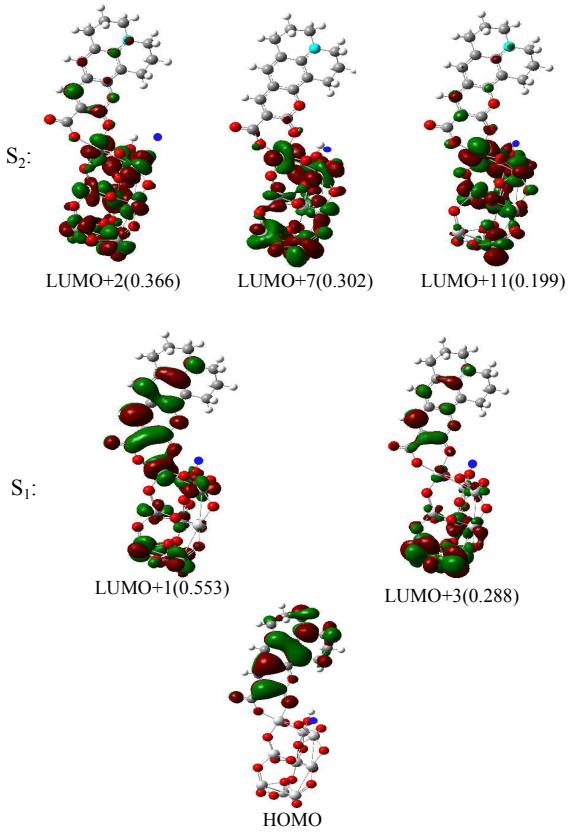

Fig. 8 The molecular orbitals related to the local excited state (S_1) and the charge transfer state (S_2)

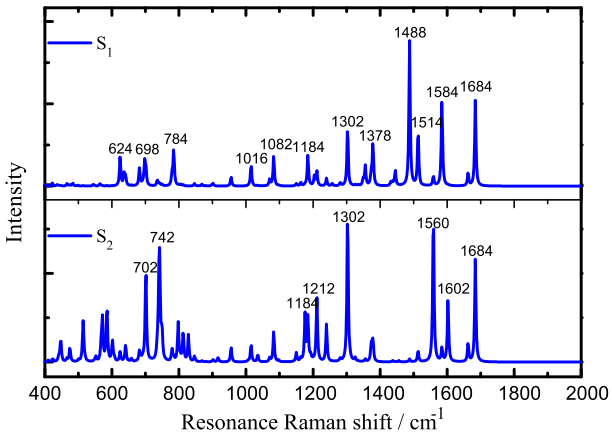

Fig. 9 The resonance Raman spectra from the local excited state and the charge transfer state

charge transfer state does not include the Herzberg-Teller (HT) effect, which has been demonstrated to be important[58,82–85]. However, the present calculations have already revealed the obviously different features of RRS from a locally excited state and charge transfer state. Definitely, the HT effect should be incorporated for the further comparison with experimental data.

4 Conclusions

Vibrationally-resolved spectral methods and quantum chemical calculations are employed to investigate the structures, normal Raman spectra (NRS) and resonance Raman spectra (RRS) of a free C343 molecule, and its compound with a small size titanium dioxide cluster Ti_9O_{18}. After the absorption of C343 on the Ti_9O_{18} cluster, it is found that the conformers with interfacial bidentate chelating and monodentate ester bonding modes are quite stable. The obtained NRS and RRS of C343 and C343-Ti_9O_{18} are sensitive to their geometric structures, therefore, both of them can be used to define their isomers and interfacial structures. The consistent RRS with experimental values have been used to define the most possible C343 isomer and C343-TiO_2 conformer. The detailed analysis further reveal that the RRS from both the free C343 and C343-TiO_2 cluster have the stronger Raman activity in a low-frequency domain than its NRS because of the obvious excited-state dynamics from the ring breathing vibrations of C343. The RRS peaks of C343-TiO_2 at the low frequencies (400-1000 cm^{-1}) dominantly correspond to the interaction between the Ti-O bond and C343 breathing vibrations, and the peaks at the high frequencies (1000-1800 cm^{-1}) are dominantly from the C343 fragment, but they show large changes comparing to those of the free C343 due to the charge redistribution and the additional adsorption modes at the interface. Furthermore, the RRS of C343-TiO_2 from a local excited state and a charge transfer state are obvious different, which can be used to clarify the charge transfer mechanism at the interface.

5 Acknowledgments

The authors acknowledge financial supports from the National Science Foundation of China (Grant Nos. 91333101 and 21133007), the 973 Program (2013CB834602) and the Scientific Research Foundation of Henan University(B2013141).

References

1 B. O'Regan and M. Grätzel, *Nature*, 1991, **335**, 737–739.
2 M. Grätzel, *Nature*, 2001, **414**, 338–344.
3 M. Grätzel, *J. Photochem. Photobiol. C: Photochem. Rev.*, 2003, **4**, 145–153.
4 A. Hagfeldt, G. Boschloo, L. Sun, L. Kloo and H. Pettersson, *Chem. Rev.*, 2010, **110**, 6595–6663.

5 J. N. Clifford, E. Martínez-Ferrero, A. Viterisi and E. Palomares, *Chem. Soc. Rev.*, 2011, **40**, 1635–1646.
6 N. A. Anderson and T. Lian, *Annu. Rev. Phys. Chem.*, 2005, **56**, 491–519.
7 Y. Tachibana, J. E. Moser, M. Grätzel, D. R. Klug and J. R. Durrant, *J. Phys. Chem.*, 1996, **100**, 20056–20062.
8 J. B. Asbury, E. Hao, Y. Wang, H. N. Ghosh and T. Lian, *J. Phys. Chem. B*, 2001, **105**, 4545–4557.
9 J. Kallioinen, G. Benkö, V. Sundström, J. E. Korppi-Tommola and A. P. Yartsev, *J. Phys. Chem. B*, 2002, **106**, 4396–4404.
10 W. R. Ducan and O. V. Prezhdo, *Annu. Rev. Phys. Chem.*, 2007, **58**, 143–184.
11 E. L. Tae, S. H. Lee, J. K. Lee, S. S. Yoo, E. J. Kang and K. B. Yoon, *J. Phys. Chem. B*, 2005, **109**, 22513–22522.
12 K. A. Walters, D. A. Gaal and J. T. Hupp, *J. Phys. Chem. B*, 2002, **106**, 5139–5142.
13 G. Ramakrishna, D. A. Jose, D. K. Kumar, A. Das, D. K. Palit and H. N. Ghosh, *J. Phys. Chem. B*, 2005, **109**, 15445–15453.
14 S. Verma, P. Kar, A. Das, D. K. Palit and H. N. Ghosh, *J. Phys. Chem. C*, 2008, **112**, 2918–2926.
15 S. Ramakrishna and F. Willig, *J. Phys. Chem. B*, 2000, **104**, 68–77.
16 S. Ramakrishna, F. Willig and V. May, *Chem. Phys. Lett.*, 2002, **351**, 242–250.
17 L. Wang, F. Willig and V. May, *J. Chem. Phys.*, 2006, **124**, 014712.
18 M. Thoss, I. Kondov and H. Wang, *Chem. Phys.*, 2004, **304**, 169–181.
19 I. Kondov, M. Thoss and H. Wang, *J. Phys. Chem. A*, 2006, **110**, 1364–1374.
20 L. G. Rego and V. S. Batista, *J. Am. Chem. Soc.*, 2003, **125**, 7989–7997.
21 W. Stier and O. V. Prezhdo, *J. Phys. Chem. B*, 2002, **106**, 8047–8054.
22 C. F. Craig, W. R. Duncan and O. V. Prezhdo, *Phys. Rev. Lett.*, 2005, **95**, 163001.
23 O. V. Prezhdo, W. R. Duncan and V. V. Prezhdo, *Prog. Surf. Sci.*, 2009, **84**, 30–68.
24 A. B. Myers, *Chem. Rev.*, 1996, **96**, 911–926.
25 A. B. Myers, *Acc. Chem. Res.*, 1997, **30**, 519–527.
26 A. M. Kelly, *J. Phys. Chem. A*, 1999, **103**, 6891–6903.
27 J. T. Hupp and R. D. Williams, *Acc. Chem. Res.*, 2001, **34**, 808–817.
28 R. L. Blackbourn, C. S. Johnson and J. T. Hupp, *J. Am. Chem. Soc.*, 1991, **113**, 1060–1062.
29 L. C. Shoute and G. R. Loppnow, *J. Chem. Phys.*, 2002, **117**, 842–850.
30 L. C. Shoute and G. R. Loppnow, *J. Am. Chem. Soc.*, 2003, **125**, 15636–15646.
31 E. J. Heller, *Acc. Chem. Res.*, 1981, **14**, 368–375.
32 A. Hagfeldt and M. Grätzel, *Acc. Chem. Res.*, 2000, **33**, 269–277.
33 X.-Y. Zhu, *J. Phys. Chem. B*, 2004, **108**, 8778–8793.
34 H. Imahori, T. Umeyama and S. Ito, *Acc. Chem. Res.*, 2009, **42**, 1809–1818.
35 A. Musumeci, D. Gosztola, T. Schiller, N. M. Dimitrijevic, V. Mujica, D. Martin and T. Rajh, *J. Am. Chem. Soc.*, 2009, **131**, 6040–6041.
36 R. R. Frontiera, J. Dasgupta and R. A. Mathies, *J. Am. Chem. Soc.*, 2009, **131**, 15630–15632.
37 W. Wu, Z. Cao and Y. Zhao, *J. Chem. Phys.*, 2012, **136**, 114305.
38 L.-L. Jiang, W.-L. Liu, Y.-F. Song, X. He, Y. Wang, H.-L. Wu and Y.-Q. Yang, *Acta Phys.-Chim. Sin.*, 2012, **28**, 2953–2957.
39 H. Li, Y. Li and M. Chen, *RSC Adv.*, 2013, **3**, 12133–12139.
40 R. S. de Armas, M. A. San-Miguel, J. Oviedo and J. F. Sanz, *Phys. Chem. Chem. Phys.*, 2012, **14**, 225–233.
41 Y. J. Yan and S. Mukamel, *J. Chem. Phys.*, 1986, **85**, 5908–5923.
42 Y. J. Yan and S. Mukamel, *J. Chem. Phys.*, 1987, **86**, 6085–6107.
43 A. C. Albrecht, *J. Chem. Phys.*, 1961, **34**, 1476–1484.
44 E. J. Heller, R. Sundberg and D. Tannor, *J. Phys. Chem.*, 1982, **86**, 1822–1833.
45 R. Bauernschmitt and R. Ahlrichs, *Chem. Phys. Lett.*, 1996, **256**, 454–464.
46 M. E. Casida, C. Jamorski, K. C. Casida and D. R. Salahub, *J. Chem. Phys.*, 1998, **108**, 4439–4449.
47 R. E. Stratmann, G. E. Scuseria and M. J. Frisch, *J. Chem. Phys.*, 1998, **109**, 8218–8224.
48 C. V. Caillie and R. D. Amos, *Chem. Phys. Lett.*, 1999, **308**, 249–255.
49 C. V. Caillie and R. D. Amos, *Chem. Phys. Lett.*, 2000, **317**, 159–164.
50 V. Barone and M. Cossi, *J. Phys. Chem. A*, 1998, **102**, 1995–2001.
51 M. Cossi, N. Rega, G. Scalmani and V. Barone, *J. Comput. Chem.*, 2003, **24**, 669–681.
52 M. J. Frisch, G. W. Trucks, H. B. Schlegel, M. A. R. G. E. Scuseria, J. R. Cheeseman, G. Scalmani, V. Barone, B. Mennucci, G. A. Petersson, H. Nakatsuji, M. Caricato, X. Li, H. P. Hratchian, A. F. Izmaylov, J. Bloino, G. Zheng, J. L. Sonnenberg, M. Hada, M. Ehara, K. Toyota, R. Fukuda, J. Hasegawa, M. Ishida, T. Nakajima, Y. Honda, O. Kitao, H. Nakai, T. Vreven, J. J. A. Montgomery, J. E. Peralta, F. Ogliaro, M. Bearpark, J. J. Heyd, E. Brothers, K. N. Kudin, V. N. Staroverov, T. Keith, R. Kobayashi, J. Normand, K. Raghavachari, A. Rendell, J. C. Burant, S. S. Iyengar, J. Tomasi, M. Cossi, N. Rega, J. M. Millam, M. Klene, J. E. Knox, J. B. Cross, V. Bakken, C. Adamo, J. Jaramillo, R. Gomperts, R. E. Stratmann, O. Yazyev, A. J. Austin, R. Cammi, C. Pomelli, J. W. Ochterski, R. L. Martin, K. Morokuma, V. G. Zakrzewski, G. A. Voth, P. Salvador, J. J. Dannenberg, S. Dapprich, A. D. Daniels, O. Farkas, J. B. Foresman, J. V. Ortiz, J. Cioslowski and D. J. Fox, *Gaussian 09, Revision B.01*, Gaussian, Inc., Wallingford, CT, 2010.
53 F. Duschinsky, *Acta Phisicochim. URSS*, 1937, 551–566.
54 W. Z. Liang, Y. Zhao, J. Sun, J. Song, S. Hu and J. Yang, *J. Phys. Chem. B*, 2006, **110**, 9908–9915.
55 H.-C. Jankowiak, J. Stuber and R. Berger, *J. Chem. Phys.*, 2007, **127**, 234101.
56 J. Guthmuller and B. Champagne, *J. Chem. Phys.*, 2007, **127**, 164507.
57 S. P. Centeno, I. López-Tocón, J. Roman-Perez, J. F. Arenas, J. Soto and J. C. Otero, *J. Phys. Chem. C.*, 2012, **116**, 23639–23645.
58 H. Ma, Y. Zhao and W. Z. Liang, *J. Chem. Phys.*, 2014, **140**, 094107.
59 S. Hamad, C. R. A. Catlow, S. M. Woodley, S. Lago and J. A. Mejías, *J. Phys. Chem. B*, 2005, **109**, 15741–15748.
60 M. J. Lundqvist, M. Nilsing, P. Persson and S. Lunell, *Int. J. Quantum Chem.*, 2006, **106**, 3214–3234.
61 Z.-W. Qu and G.-J. Kroes, *J. Phys. Chem. B*, 2006, **110**, 8998–9007.
62 Z.-W. Qu and G.-J. Kroes, *J. Phys. Chem. C*, 2007, **111**, 16808–16817.
63 W. Zhang, Y. Han, S. Yao and H. Sun, *Mater. Chem. Phys.*, 2011, **130**, 196–202.
64 R. S. de Armas, M. A. San-Miguel, J. Oviedo and J. F. Sanz, *J. Chem. Phys.*, 2012, **136**, 194702.
65 R. S. de Armas, J. Oviedo, M. A. San-Miguel and J. F. Sanz, *J. Phys. Chem. C*, 2011, **115**, 11293–11301.
66 R. S. de Armas, M. A. San-Miguel, J. Oviedo, A. Márquez and J. F. Sanz, *Phys. Chem. Chem. Phys.*, 2011, **13**, 1506–1514.
67 R. S. de Armas, J. O. López, M. A. San-Miguel, J. F. Sanz, P. Ordejón and M. Pruneda, *J. Chem. Theory Comput.*, 2010, **6**, 2856–2865.
68 K. E. Lee, M. A. Gomez, S. Elouatik and G. P. Demopoulos, *Langmuir*, 2010, **26**, 9575–9583.
69 E. Galoppini, *Coord. Chem. Rev.*, 2004, **248**, 1283–1297.
70 M. K. Nazeeruddin, R. Humphry-Baker, P. Liska and M. Grätzel, *J. Phys. Chem. B*, 2003, **107**, 8981–8987.
71 H. Tian, X. Yang, R. Chen, R. Zhang, A. Hagfeldt and L. Sun, *J. Phys. Chem. C*, 2008, **112**, 11023–11033.
72 Z.-S. Wang, K. Hara, Y. Dan-Oh, C. Kasada, A. Shinpo, S. Suga, H. Arakawa and H. Sugihara, *J. Phys. Chem. B*, 2005, **109**, 3907–3914.
73 K. Srinivas, K. Yesudas, K. Bhanuprakash, V. J. Rao and L. Giribabu, *J. Phys. Chem. C*, 2009, **113**, 20117–20126.

74 R. Argazzi, C. A. Bignozzi, T. A. Heimer, F. N. Castellano and G. J. Meyer, *Inorg. Chem.*, 1994, **33**, 5741–5749.
75 T. A. Heimer and E. J. Heilweil, *J. Phys. Chem. B*, 1997, **101**, 10990–10993.
76 R. Huber, J. E. Moser, M. Grätzel and J. Wachtveitl, *Chem. Phys.*, 2002, **285**, 39–45.
77 W. F. Zhang, Y. L. He, M. S. Zhang, Z. Yin and Q. Chen, *J. Phys. D: Appl. Phys.*, 2000, **33**, 912–916.
78 H. C. Choi, Y. M. Jung and S. B. Kim, *Vib. Spectrosc.*, 2005, **33–38**, 33.
79 J. Zhang, M. Li, Z. Feng, J. Chen and C. Li, *J. Phys. Chem. B*, 2006, **110**, 927–935.
80 H. L. Ma, J. Y. Yang, Y. B. Zhang, B. Lu and G. H. Ma, *Appl. Surf. Sci.*, 2007, **253**, 7497–7500.
81 Y. Zhao and W. Z. Liang, *J. Chem. Phys.*, 2011, **135**, 044108.
82 H. L. Ma, J. Liu and W. Z. Liang, *J. Chem. Theory Comput.*, 2012, **8**, 4474–4482.
83 J. Liu and W. Z. Liang, *J. Chem. Phys.*, 2013, **138**, 024101.
84 D. P. Chen, J. Liu, H. L. Ma, Q. Zeng and W. Z. Liang, *Sci. China Chem.*, 2014, **57**, 48–75.
85 W. Liang, H. Ma, H. Zang and C. Ye, *Int. J. Quantum Chem.*, 2014, doi:10.1002/qua.24824.